Research Square

Preprints are preliminary reports that have not undergone peer review.
They should not be considered conclusive, used to inform clinical practice,
or referenced by the media as validated information.

A Zn(II)-Organic Framework as a Fluorescent Probe for the Aqueous Phase Detection of Nitroaromatic Explosive and Cr(III) ion

Samrah Kamal
Aligarh Muslim University
Mohd Khalid (khalid215@gmail.com)
Aligarh Muslim University
M. Shahnawaz Khan
Aligarh Muslim University
M. Shahid
Aligarh Muslim University
Musheer Ahmad
Aligarh Muslim University

Research Article

Keywords: Metal-organic framework, TNP detection, Fluorescence quenching, Cr3+ sensing

Posted Date: September 29th, 2021

DOI: https://doi.org/10.21203/rs.3.rs-934804/v1

License: This work is licensed under a Creative Commons Attribution 4.0 International License.
Read Full License

Abstract

From the perspective of environment, civilian safety and human health it is utmost important to selectively and sensitively detect hazardous substances in the running water. In the last few decades, metal organic frameworks (MOFs) have been utilized for the detection of lethal substances in the aqueous phase using fluorescence method. Herein, a highly fluorescent MOF, **Zn-MOF-1**, namely, $\{[Zn_2(pydc)_2(DMF)]\cdot 2DMF\}_n$, based on the ligand pyridine-2,5-dicarboxylic acid (H_2pydc), was synthesized by employing solvothermal conditions. The **Zn-MOF-1** was thoroughly characterized by crystallographic, PXRD, elemental, FTIR, and TG analysis. Single crystal data elucidated the exact structure of **Zn-MOF-1**. Due to its better emission spectra, the fluorescence sensing behavior of **Zn-MOF-1** was checked in the aqueous medium. It was found that **Zn-MOF-1** could detect Cr^{3+} with high sensitivity and selectivity and serve as an excellent fluorescent probe for TNP among other interfering nitroaromatic compounds in aqueous media. Furthermore, a plausible sensing mechanism has been demonstrated employing UV-Visible, fluorescence, and theoretical data. The observed K_{sv} values for TNP and Cr^{3+} are 2.1×10^8 M^{-1} and 1.46×10^7 M^{-1}, respectively. Selective fluorescence quenching with high K_{sv} values and low detection limits validates the superior sensing performance shown by **Zn-MOF-1** toward TNP and Cr^{3+}. Thus, the fine-tuning of MOF for the detection of hazardous substances in wastewater is a challenging task and needs to address in future endeavors.

1. Introduction

From the point of constantly increasing pollution problems worldwide, novel functional materials have attracted considerable attention towards chemist due to its fast response time, high sensitivity, selectivity, and low limit of detection to sense the pollutants. Metal-organic frameworks (MOFs), a kind of evolving crystalline materials, comprises organic linkers and inorganic building blocks, and these rigid, stable, and emerging materials continue to be a subject of intense research [1]. Owing to their structural diversity, tunable pore size, and potential applications in a broad range of areas; for instance, drug delivery and release [2], heterogeneous catalysis [3], adsorption [4], gas storage, separation [5] and fluorescence sensing [6]. MOFs, as fluorescent probes, possess great superiorities including, low cost, simplicity, rapid response, high sensibility, liable recyclability, ease of handling and sample preparation [7]. On the other hand, the other detection methods such as atomic absorption spectroscopy, cyclic voltammetry, inductively coupled plasma mass spectrometry (ICPMS), gas chromatography – mass spectrometry, high-pressure liquid chromatography, ion mobility spectroscopy and raman spectroscopy [8] are costly, time consuming and tough to operate [9]. The abundance of fluorescent MOF materials has been scrutinized in the literature to date for sensing purpose which involves sensing of various hazardous substances such as cations-anions, volatile organic compounds, small molecules, Nitroaromatic compounds (NACs) [10]. NACs are among the most common malignant organic pollutants due to their toxic nature, highly explosive, and difficult to decompose naturally [11]. Among others, 2,4,6-trinitrophenol (TNP) is severely hazardous due to their high explosive nature, low safety coefficient, and widespread applications in fireworks, glass, matches, dyes, rocket fuels, and leather industries [12]. The effluents released by the

industries into the environment containing TNP can results in severe environmental problems. Metabolism of TNP develops picramic acid as a byproduct which shows the tenfold mutagenic activity compared to TNP [13]. Moreover, the carcinogenic activities of TNP can results in various health related issues such as headache, anemia, improper liver functions, skin irritation and so forth [14]. Hence, to decrease the adverse belongings of TNP on the atmosphere, it is reasonably necessary to evolve such kind of sensing material that is reliable, convenient and efficient, in order to detect NACs for the above concerns. Fluorescence-based chemical sensors; for instance, conjugated polymers [15], nanoparticles [16], MOF based fluorescent probes [17] are highly in demand for selective and sensitive detection of NACs.

On the flip side, the inorganic pollutant, hefty metal cations, are becoming a topical issue due to their high toxicity and bioaccumulation [18]. Among the essential heavy metal ions, detection of Cr^{3+} ion is also crucial since it significantly impacts the metabolism of carbohydrates, fats, nucleic acids, and proteins. Cr^{3+} is an essential trace element for human health. The insufficiency of Cr^{3+} might cause diabetes, cardiovascular diseases, and atherosclerosis [19]. However, Cr^{3+} in excess is still detrimental to human health, which can combine with DNA in the body and results in mutation or malignant cells [20]. Chromium is employed in industries on a large scale, for instance, steel fabrication, electroplating, tanning, paint manufacturing. Chromium waste is developed from burning coal, oxidative dyeing, cooling towers and sanitary landfills, and the use of corrosion inhibitors in water pipes [21]. The improper disposal of industrial waste containing chromium can pollute soil and water. Consequently, damaging the environment and human health. Therefore, it is essential to trace Cr^{3+} ions fastly and sensitively, as it is beneficial for the protection of environment. Hence, it remains a challenge to design and synthesize a bifunctional fluorescent MOFs to detect Cr^{3+} ion and TNP with rapid response time, high sensitivity, and selectivity in water. Following the points mentioned above, we designed and synthesized a 3-D Zn-MOF using $Zn(NO_3)_2{\cdot}6H_2O$ and planer pydc ligand, namely, $\{[Zn_2(pydc)_2(DMF)]{\cdot}2DMF\}_n$ **Zn-MOF-1**, which was fortunately manufactured through a solvothermal method. The MOF was characterized using various spectroscopic technique and the definite structure was drawn by single crystal method. The **Zn-MOF-1** can exploit as a dual fluorescent sensor to detect TNP and Cr^{3+} ion with a extremely low limit of detection in the aqueous phase. The better stability of **Zn-MOF-1** can be the reason for its better sensing ability towards the hazardous substances in the water. By its good selectivity and sensitivity in sensing, it is competitive with current sensory materials.

2. Experimental Protocols

2.1 Materials and methods

The reagents used in this paper were analytical grade and procured from trade sources and used as received. pyridine-2,5-dicarboxylic acid (pydc), zinc nitrate hexahydrate, Nitroaromatic compounds (NACs), and the metal salts of nitrate were procured from Sigma-Aldrich Chemical Co. India.

Caution

NACs are very reactive and explosives in nature and should be tested carefully and only in minute quantity. To prevent explosion, nitroaromatics were treated in safe manner.

2.2 Physical Methods

The solid state FTIR spectrum of **Zn-MOF-1** within the range of 4000 – 400 cm^{-1} on the Perkin Elmer Model spectrum GX spectrophotometer. The Melting point of the compound was checked employing open capillary method. Further, the elemental analysis was obtained from Micro-Analytical Laboratory in CDRI, Lucknow, India. Perkin Elmer λ-45 UV visible spectrophotometer was used to record the electronic spectrum of the compound. The stock solution was made in 10^{-3} M solution in aqueous phase by maintaining the 1cm length of the cuvettes. Hitachi F-2700 spectrophotometer were used to record the emission spectra. “Miniflexll X-ray diffractometer” with Cu-Kα radiation was used to determine the PXRD patterns. The thermal behavior of MOF was checked using Shimadzu TGA-50H instrument with the heating of 20˚C min^{-1} from 25˚C to 800˚C.

2.3 Single crystal X-ray data

The Single Crystal X-ray diffraction of **Zn-MOF-1** at 100 K was performed on Bruker SMART APEX CCD diffractometer. The graphite monochrome and Mo-Kα radiation (λ = 0.71073 Å) was used for X-ray data collection [22]. Employing SAINT SOFTWARE, the reduction and integration of data were created [23]. The SADABS was used for empirical absorption correction [24] and XPREP was used to investigate the space group in **Zn-MOF-1** [25]. The structure refinement was done by exploiting least-squares techniques on F^2 by employing the OLEX-2 program package [26]. Furthermore, the non-hydrogen atoms were refined with anisotropic displacement parameters. The different hydrogen positions were fixed at calculated positions and refined isotopically. The CCDC reference numbers for **Zn-MOF-1** is 2077312.

2.4 Sensing Experiments

In usual setup, the stock solution (1mM) of **Zn-MOF-1** was prepared. The 3ml aqueous solution of **Zn-MOF-1** was placed in a 1cm quartz cuvette on emission spectrophotometer. After excitation on 272 nm the fluorescence response was recorded. The incremental addition of nitro analytes and metal salts were added in the solution of **Zn-MOF-1** and the emission spectra was observed. In the entire experiment the slit width of 2 nm was kept constant for both source and detector.

2.5 Synthesis of $\{[Zn_2(pydc)_2(DMF)]\cdot 2DMF\}_n$

The **Zn-MOF-1** was synthesized by mixing 0.2 mmol (0.033 gm) of H_2pydc, 0.2 mmol (0.059 gm) of $Zn(NO_3)_2\cdot 6H_2O$ in 3mL of DMF. Then the solution was sealed in a Teflon- line stainless-steel autoclave and heated for 72h at 100˚C. After that it was gradually cooled to room temperature over 12h. The small colorless round-shaped crystals were obtained in a yield of 48%.

Yield: 48%, m.p. 315˚C, Anal.Calcd (%) for $C_{17}H_{13}N_3O_9Zn_2$: C = 52.92; H = 11.02; N = 5.51; Observed: C = 52.89; H = 11.06; N = 5.54. IR (KBr, cm^{-1}): 3438br, 2925m, 1614s, 1383s, 1281w, 763m, 533w, 423w.

3. Results And Discussions

3.1 Synthetic approach

To uncover the chemistry behind the luminescent metal organic system in terms of its sensitive and selective sensing of hazardous substance in the water. We have employed our understanding and constructed a Zn(II)-based metal organic system which is better than other MOF based materials in terms of their sensing ability using fluorescence method. Fortunately, we have successfully synthesized a fluorescent **Zn-MOF-1**, by employing a planer pydc ligand which possess various coordination modes (Scheme 1**)**. In this work we applied solvothermal method to synthesize **Zn-MOF-1**. We choose this method because of high solubility of precursors and thereby leads to the production of high-quality MOF crystals. The choice of solvent plays an important role as well. The solvent utilized in the fabrication process which may assist in binding with metal ions and thus act as a coordinating ligand or can behave as a guest solvent molecule in the environment of the complex [28]. Therefore, to look over the impact of coordination affinity towards the solvent, Junhua Luo's group carried out several reactions with distinct solvents such as DMF, DEF and DMA of H_3BPT and $Cd(NO_3)_2{\cdot}4H_2O$ [29], among which some coordination architecture have been reported; for instance, $\{[Cd_3(BPT)_2(DMF)_2]{\cdot}2H_2O\}$, which possess solvent as a coordinating agent, comparable to our designed MOF **Zn-MOF-1** in which DMF act as both coordinating ligand and guest molecule in the lattice environment (Scheme 2).

3.2 Structural explanation of Zn-MOF-1

The Single crystal x-ray data (SCXRD) was used to analyze the exact structure of **Zn-MOF-1**. The SCXRD analysis revelas that **Zn-MOF-1** crystallizes in a monoclinic system with P1 21/n1 space group. Table 1 enlisted the crystal data and different refinement parameters, and selected bond lengths, angles are given in **Table S1** of **Zn-MOF-1**. The structure of **Zn-MOF-1**, i.e., $\{[Zn_2(pydc)_2(DMF)]{\cdot}2DMF\}_n$ is assembled by the repeating units of binuclear Zn(II) species. The labeled molecular structure of **Zn-MOF-1** is dispensed in Fig. 1. The interesting feature of **Zn-MOF-1** is that the two different Zn atoms, Zn1 and Zn2, exist in the structure in two different coordination environments. Each Zn1 atom is coordinated by one N- atom of pydc ligand, four O- atom from four different pydc ligands, and one O- atom of DMF ligand. Zn1 acquire distorted octahedral geometry (Fig. 2a) with O4, O9, N1, O1 form the equatorial plane, while O8 and O5 occupying the axial position. Few important bond angles that describe the order of distortion around Zn1 atom are found as O9-Zn1-O4 = 166.81(6)˚, O1-Zn1-N1 = 170.13(7)˚, O5-Zn1-O8 = 177.78(6)˚, it supports the distorted octahedral geometry of **Zn-MOF-1** [30]. On the other hand, similar coordination environment is found in Zn2 in terms of coordination to the pydc ligands. The coordination environment around Zn2 is filled by one N- atom of pydc ligand and four O- atoms of carboxylate moiety from four different pydc ligands with five coordination sites. The five-coordinated system can attain either triangular bipyramidal

(tbp) geometry or square pyramidal (sq-py) geometry of Zn(II) ion. The Addison and co-workers introduced t parameter to distinguish between these two geometries [31]. The t parameter is in the range of 0–1 and at the utmost values giving perfect sq-py or tbp geometry, respectively. The closer the value of t to 0, the more relatable it is to sq-py geometry. We can calculate this parameter by applying the difference between the two largest coordination center angles and divide it by 60˚. Our calculation shows that Zn(2) has a distorted sq-py geometry with t = (159.25-147.84)/60 = 0.19 (Fig. 2b). The quasi-square plane i.e., base is formed by O4, O6, O7, and N2. The top of the pyramid i.e., apex is formed by O2. The important bond angles are obtained as O4-Zn2-N2 = 147.84(7)˚ and O7-Zn2-O6 = 159.25(7)˚. The oxygen (O4) of the same pydc ligand bridges the Zn1 and Zn2 atom. The bond angle between Zn2 with its neighboring atom is N2-Zn2-O4 = 147.84(7)˚, O7-Zn2-O4 = 100.38(6)˚, O6-Zn2-O7 = 159.25(7)˚, N2-Zn2-O2 = 110.59(7)˚; it also supports the distorted sq-py. For the sake of clarity, two uncoordinated DMF molecules in the lattice environment are squeezed. It should be noteworthy that, in **Zn-MOF-1** pydc ligand exhibits two distinct coordination modes as shown in Fig. 2c. In mode-I, μ_2-η^1:η^1 bridging mode is adopted by one carboxylate group. In contrast, the O-atom of the second carboxylate group and N-atom of pyridine adopts the μ_1-η^1:η^1 chelating mode, and the other O-atom of the same carboxylate group is present in μ_1:η^1 bridging mode, while in mode-II pydc shows similar coordination modes as that of mode-I except for the second carboxylate group, which adopts μ_1-η^1:η^2 bridging mode. In both cases, the whole pydc ligands act as a μ_4- bridge to bind four different Zn(II) atoms in adjoining chains, resulting in a three-dimensional network structure (Fig. 3) [32, 33].

Table 1
Crystal structure and refinement data for **Zn-MOF-1**.

Compound	**Zn-MOF-1**
Empirical formula	C_{17} H_{13} N_3 O_9 Zn_2
Formula weight	534.10
Crystal color	Colorless
Temperature/K	100(2)
Crystal system	Monoclinic
Space group	P 1 21/n 1
a/Å	14.0774(10)
b/Å	12.1211(9)
c/Å	14.6325(10)
α/°	90
β/°	106.079(2)
γ/°	90
Volume/$Å^3$	2399.1(3)
Z	4
$\rho_{calc}g/cm^3$	1.4786
μ/mm^{-1}	2.047
F(000)	1075.0356
Crystal size/mm^3	0.37
Radiation	Mo-Kα
Independent reflections	5975
WR_2(all)	0.0896
WR_2	0.0841
Final R Indexes [I >= 2σ(I)]	0.0294
Final R indexe(all data)	0.0363
Θ_{min}	2.18

Compound	Zn-MOF-1
Θ_{max}	21.91

3.3 FTIR, UV-Visible, PXRD and TG analysis of Zn-MOF-1

FT-IR spectrum of **Zn-MOF-1** is given in Fig. 4a. The broadband observed at 3438 cm^{-1} can be consigned to the v(C-H) pyridyl ring stretching vibration. Again, the weak band at 2925 cm^{-1} is characteristic of the v(C-H) vibrations of the coordinated DMF molecule. The absence of characteristics band at around 1700 cm^{-1} which is assignable to –COOH groups designate that all carboxyl groups is completely deprotonated in **Zn-MOF-1** upon reaction with metal ion [34]. For **Zn-MOF-1**, the two strong bands at 1614 cm^{-1} and 1383 cm^{-1} (**Scheme S1**), corresponding to the stretching vibrations of asymmetric and symmetric carboxyl groups, respectively [35]. The weak band at 1281 cm^{-1} are assigned to v(C-O) vibrations and the absorption band observed at 763 cm^{-1} are due to δ(O-C-O) vibrations of the pydc [36]. The absorption at 533 cm^{-1} corresponds to v(Zn-O) vibration, and the band in weak intensity at 423 cm^{-1} consigned to the v(Zn-N) vibration [37]. The infrared spectra of **Zn-MOF-1** are compatible with its structural features as resolved by SCXRD. The absorption spectrum of **Zn-MOF-1** exhibited well resolved absorption band at 272 nm which is assignable to intraligand (n→π*, π→π*) transition. **Zn-MOF-1** doesn't show any d-d transition due to the closed shell d^{10} configuration as illustrated in Fig. 4b.

Thermal gravimetric analysis (TGA) was performed in presence of N_2 atmosphere, to inspect the thermal disintegration of **Zn-MOF-1.** The model pattern of TG curve exhibits two decomposition steps as shown in Fig. 4c. In very first step, TG curve displays the weight loss of 27.36% at 380˚C, corroborates the loss of two uncoordinated DMF in the lattice (Calc.: 27.50%), while in case of second step it exhibits weight loss of 76.26% at 550˚C which is corresponds to the loss of one coordinated DMF and two units of pydc ligand (Calc.: 76.52%). Then, no changes were found from 550˚C-800˚C and the final product left may be the metal residue. Additionally, the PXRD investigation were done on **Zn-MOF-1** to affirm the phase purity of the sample. The simulated and as-synthesized patterns are quite similar to each other as display in Fig. 5. The PXRD patterns of **Zn-MOF-1** was also recorded before and after immersing the sample in water for 24h. Both the pattern is almost identical confirming the robust nature and structural integrity of **Zn-MOF-1** [38].

3.4 Fluorescence ability of Zn-MOF-1

After excitation at 272 nm the emission spectrum of **Zn-MOF-1** in solution state shows a sharp intense peak at 385 nm Fig. 4b. The Zn(II) ions possess d^{10} configuration, thus it is not easily get oxidize or reduce, it indicates the absence of MLCT and LMCT behavior of **Zn-MOF-1** [39]. Consequently, the band of **Zn-MOF-1** can be consigned to intraligand fluorescence emissions. Additionally, to check out either the emission spectra are based only on ligand or depend on the entire moiety of **Zn-MOF-1**, the emission spectra of free ligand pydc upon excitation at 270 nm shows a moderate peat at 345 nm (Fig. 6.).

Accordingly, it could be deduced that intense emission spectrum of **Zn-MOF-1** doesn't depend merely on ligand moiety instead its entire moiety is the reason behind the intense emission, thus **Zn-MOF-1** is a fluorescent material. This inspire us to explore its potential application in the field of nitroaromatic compounds sensitive sensing and some other vital and lethal metal ions.

3.5 Selective and sensitive recognition of TNP

In order to understand the potential application of **Zn-MOF-1** to sense a minute amount of nitro explosives, fluorescence-quenching titration was implemented by the incremental addition of nitro analytes to **Zn-MOF-1** in H_2O. For fluorescence sensing experiment, specified nitro aromatics compounds were selected: TNP (2,4,6-trinitrophenol), ONP (2-nitrophenol), ONA (2-nitroaniline), MNA (3-nitroaniline), MDNB (1,3-dinitrobenzene). The fluorescence intensity of **Zn-MOF-1** had a little effect on incremental addition of ONA, MNA, and MDNB (**Fig. S1-S2, ESI**), except for ONP, which shows considerable quenching behavior (**Fig. S2b, ESI**). Impressively, **Zn-MOF-1** showed good sensing behavior and high fluorescence quenching (95%) for TNP on incremental addition of 10^{-3}M (50µL) analyte (Fig. 7b**).** The marvelous fluorescence quenching of 54% was observed at a very little concentration of TNP i.e., 0.12 ppb in H_2O (details in ESI). As far as we know, **Zn-MOF-1** shows the highest quenching efficiency as compare to that of reported MOFs [40] for sensitive sensing of TNP employing **Zn-MOF-1 (**Table 2**)**. The quenching efficiencies of the selected analytes in descending order are as follows: TNP (95%) > ONP (87%) > MDNB (50%) > MNA (47%) > ONA (41%) (Fig. 7d**).** This indicates a strong interaction between TNP and **Zn-MOF-1** with a detection limit of 0.12 ppb. This signify that **Zn-MOF-1** exihibits super sensitivity for TNP detection in the aquatic phase, which is vital for environmental application purpose [41]. Using Stern-Volmer (S-V) equation [42] (details in ESI) we analyzed the quenching efficiencies of all the analytes to discover the cause behind the quenching mechanism for the selective and sensitive sensing of TNP. The plots with TNP and ONP show a linear increase at low concentration, which deviates from linearity and turn in an upwards direction with increasing concentrations. Whereas the other nitro aromatic analytes showed only linear trends in the S-V plots (Fig. 7c**)**. A 3-D model of the S-V plots of **Zn-MOF-1** for different nitro analytes in water is shown (Fig. 8). On the other hand the linear fitting plot (R^2 = 0.97) displays the significant quenching ability of **Zn-MOF-1** towards TNP in water with Stern-Volmer quenching constant K_{sv} of 2.1×10^8 for TNP and among the reported MOFs this is the highest value obtained for selective detection of TNP till date [43]. Two possible mechanisms for quenching the fluorescence intensity of electron-rich **Zn-MOF-1** by electron-deficient TNP can be suggested on the basis of steady-state fluorescence measurements. It includes (1) photo-induced electron transfer (PET) mechanism and (2) fluorescence resonance energy transfer (FRET) mechanism. The highly selective detection of TNP by **Zn-MOF-1** might be assigned to PET mechanism. In general, the lowest unoccupied MOs (LUMO) of nitro analyte (electron-deficient) lies between the valence band (VB) and conduction band (CB) of the MOFs [44]. Upon excitation, the excited electron resided in the CB of **Zn-MOF-1** can easily transfer to the LUMO of electron-deficient analytes. Therefore, there is quenching in fluorescence intensity of **Zn-MOF-1**. However, in case of analytes having electron-rich systems, the LUMO lies above the CB of the MOFs, excited-state electrons from the LUMO of the analytes will be transferred to the CB of the MOFs which

leads to the enrichment of the fluorescence intensity. This was well elaborated by various research articles published in the literature. Mukul et al. reported the insight of PET mechanism by employing the theoretical calculations such as DFT. In this article the 2,6-pyridine dicarboxylic acid (pda^{2-}) ligand has been employed for the formation of three Ln-based MOF materials. The DFT calculations can be employed to calculate the HOMO-LUMO energy gap. The energy gap calculated using DFT does not in good agreement of PET mechanism which means that the PET mechanism is not the solely mechanism responsible for the sensitive and selective detection of TNP. This was also well established in the few other articles in which author used DFT calculations for confirming the mechanism associated with the sensitive and selective detection of nitro analytes [45]. Though, the fluorescence quenching for all other nitro analytes is not in line with their LUMO energy trend except TNP, this indicate that there were some other reasons for drastic quenching which synchronized with electron transfer. The FRET mechanism transfer resonance energy from fluorophore to non-emissive analyte. The absorption bands of the nitro analytes must overlap effectively with the emission band of the fluorophore [46]. To examine this, the normalized emission spectra and UV spectra of the **Zn-MOF-1** and for all the nitro analytes were recorded. The overlap graph was plotted between the relative intensity and the wavelength. As shown in Fig. 9 it is found that TNP showed maximum overlap with the fluorescence emission spectrum of **Zn-MOF-1**. On the other hand, it was relatively less or almost no overlap was found for other nitro analytes. This is in plausible accordance with the high quenching efficiency observed for TNP as compare to other nitro analytes. Consequently, it is eminent in TNP that it involves both electron and energy-transfer mechanisms where as only electron-transfer mechanisms could employ by other nitro analytes. Thereby collaborative involvement of such processes, *viz.* PET and FRET, that may lead to the enhancement of quenching efficiency of TNP with a very good detection-sensitivity limit. Furthermore, with the help of X-ray structure it was well established that there is no evidence of porosity in the structure of **Zn-MOF-1**. Hence the trapping of nitroaromatic analytes on the pores of **Zn-MOF-1** was nullified. Moreover, the identical PXRD patterns of **Zn-MOF-1**, before and after soaking in the solution of TNP for 24h specify that there is no evidence of degradation of **Zn-MOF-1** after immersing it in TNP as specified in Fig. 5 which authenticate the robust nature and stability of the MOF. The particular **Zn-MOF-1** can be used for different cycle of fluorescence sensing and to trace the TNP in water.

3.6 Selective and sensitive detection of Cr^{3+}

To check the sensing behavior of **Zn-MOF-1**, we prepared stock solution of different metal ions $M(NO_3)_x$ (M = Na^+, K^+, Ba^{2+}, Sr^{2+}, Mn^{2+}, Co^{2+}, Ca^{2+}, Zn^{2+}, Mg^{2+}, Sn^{2+}, Cd^{2+}, Pb^{2+}, Cu^{2+}, Hg^{2+}, Cr^{3+}, Cr^{6+}) in aqueous phase and gradually it was added to the aqueous solution of **Zn-MOF-1** and then the fluorescence spectra were recorded. It was detected that the fluorescence intensity was moderately enhanced in Zn^{2+}, Sr^{2+}, Na^+, Mn^{2+}, Co^{2+}, Ca^{2+}, Mg^{2+}, Cr^{6+}, Ba^{2+}, Sn^{2+}, Cd^{2+}, Pb^{2+}, Cu^{2+}, and K^+ ions except in the case of Hg^{2+} ion which shows a mild quenching behavior. As shown in Fig. 10a, a notable quenching was detected by Cr^{3+} ion. The quenching efficiency was calculated to be 43% after the addition of only 10^{-3}M (50µl) of Cr^{3+} ions. The quenching efficiency affiliated with Hg^{2+} ions was 11% which is the highest value in

comparative to other metal ions, Fig. 11a. This suggested that **Zn-MOF-1** can be used selectively for the sensing of Cr^{3+} ions in an aqueous solution. From the practical point of view selectivity in sensing is a very crucial factor in biological and environmental systems where numerous metal ions may coexist. To further explore the sensitivity of **Zn-MOF-1** as a Cr^{3+} sensor the fluorescence quenching titrations experiment were done by gradual addition of different concentrations of Cr^{3+} ions. Fluorescence intensity of **Zn-MOF-1** moderately decreased as the concentration of Cr^{3+} ion increases (Fig. 10b). Moreover, the Stern-Volmer constant, $K_{sv} = 1.46\times10^{7}$ obtained from linear fitting of the plot ($R^2 = 0.93$) (details in ESI). **Zn-MOF-1** exhibits the highest K_{sv} value reported for selective and sensitive sensing of Cr^{3+} ion **(**Table 3**).** Competitive experiments were carried out to explore the selectivity for sensing Cr^{3+} ions over various interfering metal cations. As shown in Fig. 11b, upon the addition of Cr^{3+} ions to the mixture of **Zn-MOF-1** and other interfering cations, it was observed that the fluorescence is remarkably quenched, indicating that **Zn-MOF-1** can selectively and effectively detect Cr^{3+} ion. It was illustrating that Cr^{3+} ions can still be sensed when it is accompanied by other metal ions.

As reported in previous literature, the quenching mechanisms of the fluorescent MOFs of various metal ions mainly attributed to (i) the structure of MOF being collapsed by the metal ions; (ii) exchange of cations between the metal centers of MOFs and the objective cations; (iii) competetive absorption and fluorescence resonance energy transfer **(FRET)** between fluorophores in MOFs and incoming metal ions [47]. The following experiments were performed to elucidate the mechanism of **Zn-MOF-1** as a sensor towards Cr^{3+} ion through quenching effects. PXRD patterns of **Zn-MOF-1** were recorded before and after soaking in the solution of Cr^{3+} for 24h to authenticate the extra stability of **Zn-MOF-1 (**Fig. 5**).** Secondly, Considering the neutral framework of **Zn-MOF-1**, it is not possible that the fluorescence sensing results from cations exchange. As shown in Fig. 12 the UV-visible absorption spectrum of various metal cations was measured, which showed that solely Cr^{3+} significantly overlapped with the excitation band of **Zn-MOF-1**, which suggested that the competitive energy absorption between **Zn-MOF-1** excitation and Cr^{3+} ion absorption probably happened and resulted in fluorescence quenching of **Zn-MOF-1**. Therefore, it can be deduced that the fluorescence quenching mechanism of **Zn-MOF-1** for sensing of Cr^{3+} can be attributed to both competitive energy absorption and FRET.

To calculate the detection limit, TNP (5–50µl, 1mM stock solution) and Cr^{3+} (50–300µl, 1mM stock solution) were added to **Zn-MOF-1**, and noted the equivalent fluorescent intensities by plotting the graph between fluorescence intensity and increasing concentration of the analyte, then calculated the slope (m) of the analogue graph **(Fig S3, S4, ESI).** Moreover, from five blank measurements standard deviation (σ) was also calculated of **Zn-MOF-1 (Table S2, S3, S4, ESI)**, and the detection limit of **Zn-MOF-1** was calculated by employing the formula: Detection limit = (3σ/m). TNP has detection limit of 0.12 ppb while 0.62 ppb was found in the case of Cr^{3+}.

Table 2
Selected MOF with TNP sensing and their K_{sv} Value.

Fluorescent sensing Materials	Analyte	Ksv(M^{-1})	Detection limit	Ref.
$[Zr_6O_4(OH)_4(BTDB)_6]\cdot 8H_2O\cdot 6DMF$	TNP	2.49×10^4	1.63ppm	48
$[Eu_2(L)_2(DMA)_2]n\cdot nH_2O$	TNP	3.58×10^4	4.66×10^{-4}mM	49
Bio-MOF-1	TNP	4.6×10^4	2.9ppb	50
[Tb(1,3,5-BTC)]	TNP	3.41×10^4	8.1×10^{-8} M	51
UiO-68@NH_2	TNP	5.8×10^4	0.4 ppm	52
Y-MOF:Eu	TNP	3.21×10^4	4μM	53
Y-MOF:Tb	TNP	$3.19\ 10^4$	6.5μM	53
Zn-MOF-1	TNP	2.1×10^8	0.12ppb	**This Work**

Table 3
Selected MOF with Cr^{3+} sensing and their K_{sv} Value.

Fluorescent sensing Materials	Analyte	Ksv(M^{-1})	Detection limit	Ref.
$[Zn_2(TCBPDC)_{0.5}(H_2O)_2]_n$	Cr^{3+}	7.32×10^3	0.56ppm	54
$[Eu_2(tpbpc)_4\cdot CO_3\cdot 4H_2O]\cdot DMF\cdot solvent$	Cr^{3+}	5.14×10^2	3.64ppm	55
$[Tb(hfac)_3(NITPh\text{-}Pa)_2][0.5CH_3(CH_2)_5CH_3]$	Cr^{3+}	1483.82	2.34ppm	56
$[Zn\ (tbda)]_n$	Cr^{3+}	2.68×10^3	9.36ppm	57
$[CH_3\text{-}dpb]_2[Mg_3(1,4NDC)_4(\mu H_2O)_2(CH_3OH)(H_2O)]\cdot 1.5H_2O$	Cr^{3+}	0.15×10^5	960ppm	58
$Zn_3(bpdc)_2(pdc)\ (DMF)\cdot 6DMF$	Cr^{3+}	3.870×10^3	25.1ppm	59
Zn-MOF-1	Cr^{3+}	1.46×10^7	0.62ppb	**This work**

4. Conclusion

In summary, we successfully constructed and structurally characterized a fluorescent 3D **Zn-MOF-1**. The MOF was synthesized to explore sensing ability towards different hazardous substances. Using slow evaporation method, the MOF was synthesized and with the help SCXRD the exact structure of MOF was confirmed. The PXRD pattern and TG analysis reveals the bulk purity as well as thermal stability of the

Zn-MOF-1. Significantly, **Zn-MOF-1** displays strong fluorescence emission and can be used as a potential fluorescent probe for efficiently detecting TNP and Cr^{3+} ion in aqueous solution. The detection limit of **Zn-MOF-1** towards TNP and Cr^{3+} were calculated with the values of 0.12 ppb and 0.62 ppb, respectively. Furthermore, the possible fluorescence quenching mechanism of **Zn-MOF-1** for TNP and Cr^{3+} were also elucidated. Consequently, the present study revealed that fluorescent **Zn-MOF-1** can be rationally constructed and scrutinized as a potential fluorescent sensing material for multi-functional applications in future endeavors.

References

1. M.S. Khan, M. Khalid, M. Shahid, Polyhedron **196**, 114984 (2021)

2. K.M.L. Taylor-Pashow, J.D. Rocca, Z.G. Xie, S. Tran, W. Lin, J. Am. Chem. Soc. **131**, 14261 (2009).

3. L. Ma, J.M. Falkowski, C. Abney, W. Lin, Nat. Chem. **2**, 838 (2010).

4. M.S. Khan, M. Khalid, M. Shahid, **Mater. Adv. 1,** 1575 (2020).

5. R. Banerjee, H. Furukawa, D. Britt, C. Knobler, M. O'Keeffe, O.M. Yaghi, J. Am. Chem. Soc. **131**, 3875 (2009).

6. K. Iman, M.N. Ahamad, A. Ansari, H. A. Saleh, M. S. Khan, M. Ahmad, M. Shahid RSC Advances 11 16881 (2021).

7. L.E. Kreno, K. Leong, O.K. Farha, M. Allendorf, R.P. Van Duyne, J.T. Hupp, Chem. Rev. **112**, 1105 (2012).

8. X.Y. Xu, B. Yan, ACS Appl. Mater. Interfaces **7**, 721 (2015).

9. L. Zhang, Z. Kang, X. Xin, D. Sun, CrystEngComm **18**, 193 (2016).

10. L.E. Kreno, K. Leong, O.K. Farha, M. Allendorf, R.P.V. Duyne, J.T. Hupp, Chem. Rev. **112**, 1105 (2012).

11. Z.S. Qin, W.W. Dong, J. Zhao, Y.P. Wu, Q.C. Zhang, D.S. Li, Inorg. Chem. Front. **5**, 120 (2018).

12. S.S. Nagarkar, A.V. Desai, S.K. Ghosh, Chem. Commun. **50**, 8915 (2014).

13. K.M. Wollin, H.H. Dieter, Arch. Environ. Contam. Toxicol. **49**, 18 (2005).

14. D. Udhayakumari, S. Velmathi, P. Venkatesan, S.P. Wu, Anal. Methods **7**, 1161, (2015).

15. Y. Salinas, R. Martinez-Manez, M.D. Marcos, F. Sancenon, A.M. Costero, M. Parraad, S. Gil, Chem. Soc. Rev. **41**, 1261 (2012).

16. D. Gao, Z. Wang, B. Liu, L. Ni, M. Wu, Z. Zhang, Anal. Chem. **80**, 8545 (2008).

17. J. Lei, R. Qian, P. Ling, L. Cui, H. Ju, Trends Anal. Chem. **58**, 71 (2014).

18. L. You, D.J. Zha, E.V. Anslyn, Chem. Rev. **115**, 7840 (2015).

19. T. Yang, X.Y. Zhang, X.X. Zhang, M.L. Chen, J.H. Wang, ACS Appl. Mater. Interfaces **7**, 21287 (2015).

20. E.A. Katayev, Y.A. Ustynyuk, J. L. Sessler, Coord. Chem. Rev. **250**, 3004 (2006).

21. K.S. Subramanian, Anal. Chem. **60**, 11 (1988).

22. J. A. Ibers, W.C. Hamilton, International Tables for X-ray Crystallography, Kynoch Press, Birmingham, England, 1974, vol. IV. 26 SMART & SAINT Software Reference manuals, Version 6.45, Bruker Analytical X-ray Systems, Inc., Madison, WI, 2003.

23. SMART & SAINT, Software Reference Manuals, Version 6.45 (Bruker Analytical X-ray Systems, Inc., Madison, (2003).

24. W.P. Wu, J. Wu, J.Q. Liu, M. Trivedi, A. Kumar, RSC Adv. **7**, 54522 (2017).

25. A.W. Addison, T.N. Rao, J. Reedijk, J. Van Rijn, G.C. Verschoor, J. Chem. Soc. Dalton Trans. 1349 (1984).

26. O.V. Dolomanov, L.J. Bourhis, R.J. Gildea, J.A.K. Howard, H. Puschmann, J. Appl. Cryst. **42**, 339 (2009) (b) L.J. Bourhis, O.V. Dolomanov, R.J. Gildea, J.A.K. Howard, H. Puschmann, Acta Cryst. **71**, 59 (2015).

27. Q.B. BO, J.J. Pang, H.Y. Wang, C.H. Fan, Z.W. Zhang, Inorg. Chim. Acta **428**, 170 (2015).

28. A.A. Yakovenko, Z. Wei, M. Wriedt, J.R. Li, G.J. Halder, H.C. Zhou, Cryst. Growth Des. **14**, 5397 (2014).

29. L. Li, S. Wang, T. Chen, Z. Sun, J. Luo, M. Hong, Cryst. Growth Des. **12**, 4109 (2012).

30. S. Kamal, M. Khalid, M.S. Khan, M. Shahid, M. Ashafaq, I. Mantasha, M.S. Ahmad, M. Ahmad, M. Faizan, S. Ahmad, Inorg. Chim. Acta **512**, 119872 (2020).

31. A.W. Addison, T.N. Rao, J. Reedijk, J. Van Rijn, G.C. Verschoor, J. Chem. Soc. Dalton Trans. 1349 (1984).

32. M.S. Khan, M. Khalid, M.S. Ahmad, S. Kamal, M. Shahid, M. Ahmad, J. Biomol. Struct. Dyn. (2020). DOI: 10.1080/07391102.2021.1924263.

33. M.S. Khan, M. Khalid, M.S. Ahmad, M. Ahmad, M. Ashafaq, R. Uddin, R. Arif, M. Shahid, J. Mol. Struct. **889**, 1175 (2019).

34. M.S. Ahmad, M. Khalid, M.S. Khan, M. Shahid, M. Ahmad, J. Struct. Chem. **61**, 533 (2020).

35. M. S. Khan, M. Khalid, M. S. Ahmad, M. Shahid, M. Ahmad, Res. Chem. Intermed., **46** 2985 (2020).

36. A.T. Çolak, O.Z. Yeşilel, O. Büyükgüngör, J. Mol. Struct. **68**, 991 (2011).

37. M. S. Khan, M. U. Hayat, M. Khanam, H. Saeed, M. Owais, M. Khalid, M. Shahid, M. Ahmad J. Biomol. Struct. Dyn., **39**, 4037 (2021).

38. M.S. Khan, M. Khalid, M. Shahid, **RSC Adv. 11**, 2630 (2021).

39. L. Wen, Z. Lu, J. Lin, Z. Tian, H. Zhu, Q. Meng, Cryst. Growth Des. **7**, 93 (2007).

40. Z. Hu, B.J. Deibert, J. Li, Chem. Soc. Rev. **43**, 5815 (2014).

41. D. Li, J. Liu, R.T.K. Kwok, Z. Liang, B.Z. Tang, J. Yu, Chem. Commun. **48**, 7167 (2012).

42. E. Barea, C. Montoro, J.A.R. Navarro, Chem. Soc. Rev. **43**, 5419 (2014).

43. Z. Hu, B.J. Deibert, J. Li, Chem. Soc. Rev. **43**, 5815 (2014).

44. M.S. Khan, M. Khalid, M.S. Ahmad, M. Shahid, M. Ahmad, Dalton Trans. **48**, 12918 (2019).

45. (a) M. Raizada, F. Sama, M. Ashafaq, M. Shahid, M. Ahmad, Z.A. Siddiqi, J. Mater. Chem. C **5**, 9315 (2017); (b) M. Ashafaq, M. Khalid, M. Raizada, M. S. Ahmad, M. S. Khan, M. Shahid, M. Ahmad**, J. Inorg. Organomet. Poly Mat.. 30**, 4496 (2020).

46. J. Wang, J. Mei, W. Yuan, P. Lu, A. Qin, J. Sun, Y. Ma, B.Z. Tang, J. Mater. Chem. **21**, 4056 (2011).

47. (a) S. Dang, E. Ma, Z.M. Sun, H. Zhang, J. Mater. Chem. **22**, 16920 (2012); (b) Q. Tang, S. Liu, Y. Liu, J. Miao, S. Li, L. Zhang, Z. Shi, Z. Zheng, Inorg. Chem. **52**, 2799 (2013); (c) S.T. Zhang, J. Yang, H. Wu, Y.Y. Liu, J.F. Ma, Eur. J. Chem. **21**, 15806 (2015); (d) C.X. Yang, H.B. Ren, X.P. Yan, Anal. Chem. **85**, 7441 (2013).

48. S.K. Mostakim, S, Biswas, CrystEngComm **18**, 3104 (2016).

49. X. Wang, P. Yan, Y. Li, G. An, X. Yao, G. Li, Cryst. Growth Des. **17**, 2178 (2017).

50. B. Joarder, A.V. Desai, P. Samanta, S. Mukherjee, S.K. Ghosh, Chem. Eur. J. **21**, 965 (2015).

51. J.D. Xiao, L.G. Qiu, F. Ke, Y.P. Yuan, G.S. Xu, Y.M. Wang, X. Jiang, J. Mater. Chem. A. **1**, 8745 (2013).

52. S.S. Nagarkar, A.V. Desai, P. Samanta, S.K. Ghosh, Dalton Trans. **44**, 15175 (2015).

53. D.K. Singha, P. Majee, S.K. Mondal, P. Mahata ,RSC Adv. **5**, 102076 (2015).

54. J. Ma, Q. Guo, T. Ma, L. Zhou, J. Yang, Q.F. Yang, New J. Chem. **44**, 7293 (2020).

55. J. Liu, G. Ji, J. Xiao, Z. Liu, Inorg. Chem. **56**, 4197 (2017).

56. S.L. Yang, R.R. Wang, X.J. Jin, C.X. Zhang, Q.L. Wang, Polyhedron **144**, 101 (2018).

57. X. Liang, Y. Jia, Z. Zhan, M. Hu, Appl. Organomet. Chem. **33**, (2019).

58. Z.F. Wu, L.K. Gong, X.Y. Huang,* Inorg. Chem. **56**, 7397 (2017).

59. X. Meng, M.J. Wei, H.N. Wang, H.Y. Zang , Z.Y. Zhou , Dalton Trans. **47**, 1383 (2018).

Figures

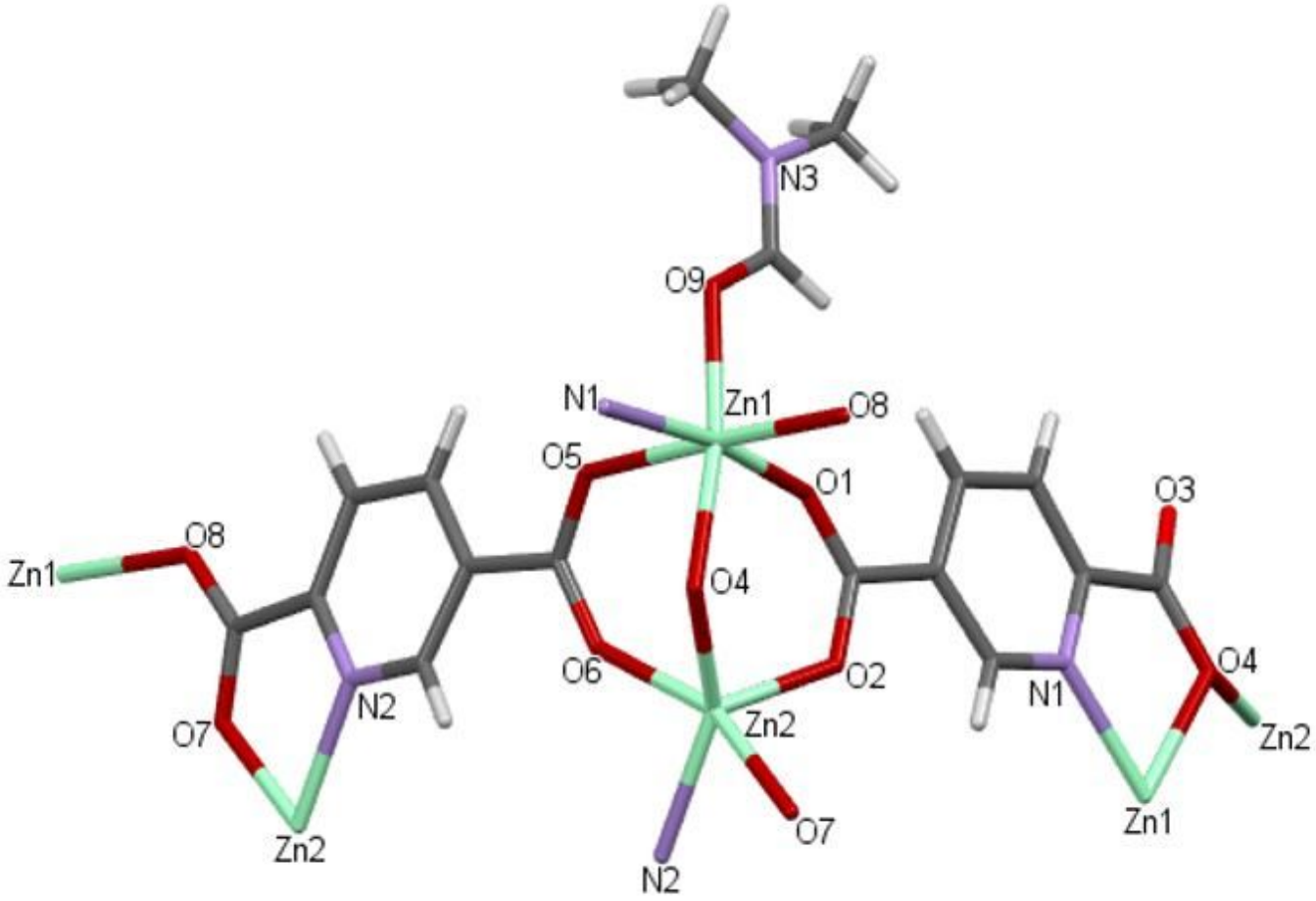

Figure 1

Labelled Molecular structure of Zn-MOF-1.

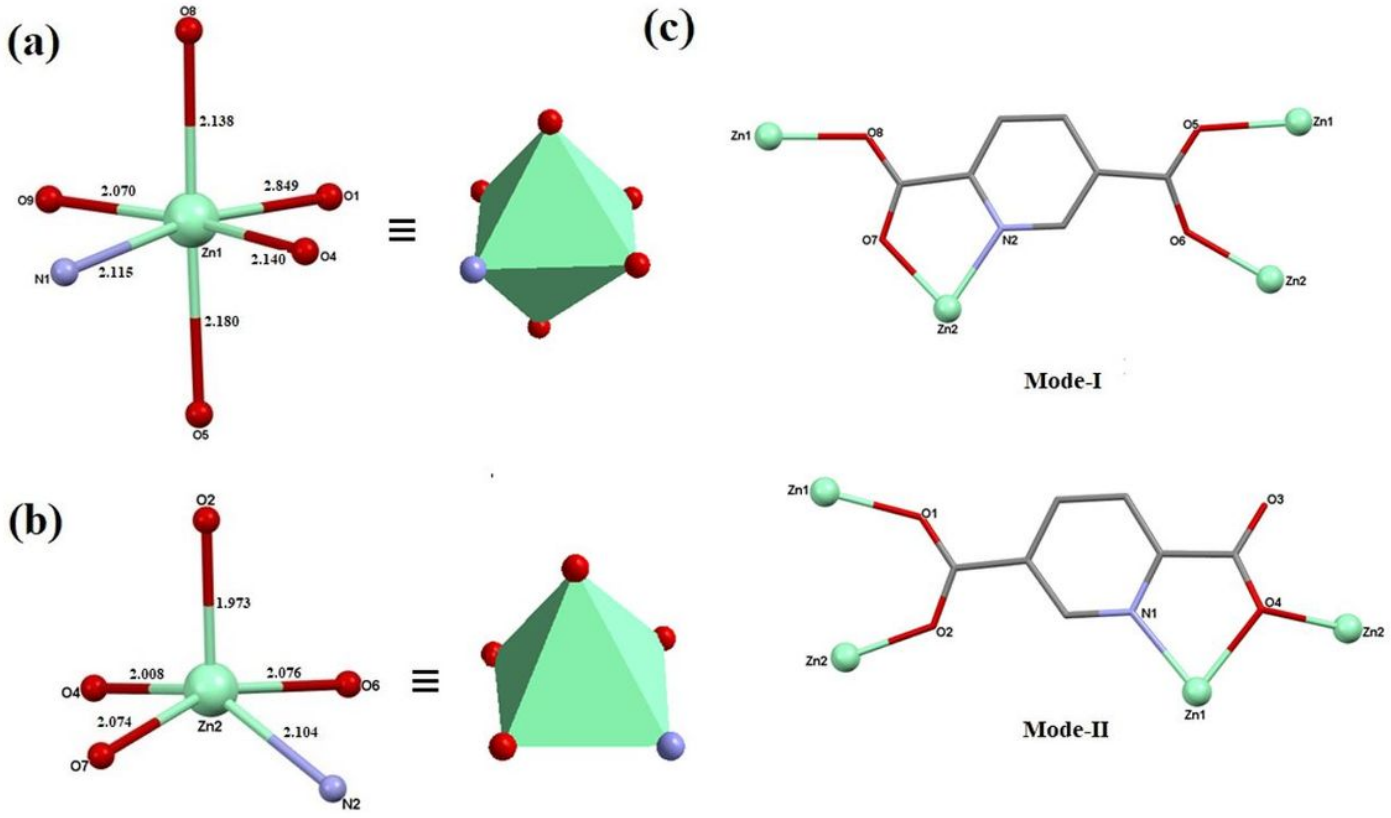

Figure 2

Six (a) and Five (b) coordinated geometry of Zn-MOF-1with bond length (in Å), (c) Distinct coordination modes of pydc2- in Zn-MOF-1.

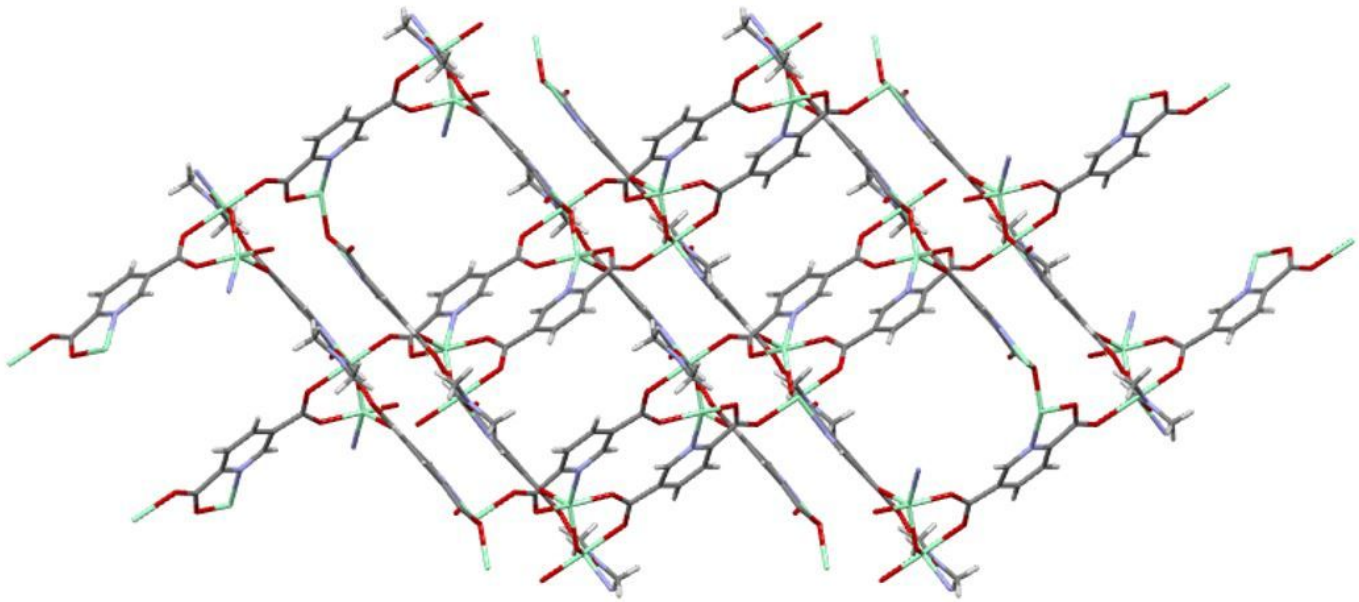

Figure 3

3D Network of Zn-MOF-1 viewed along [010].

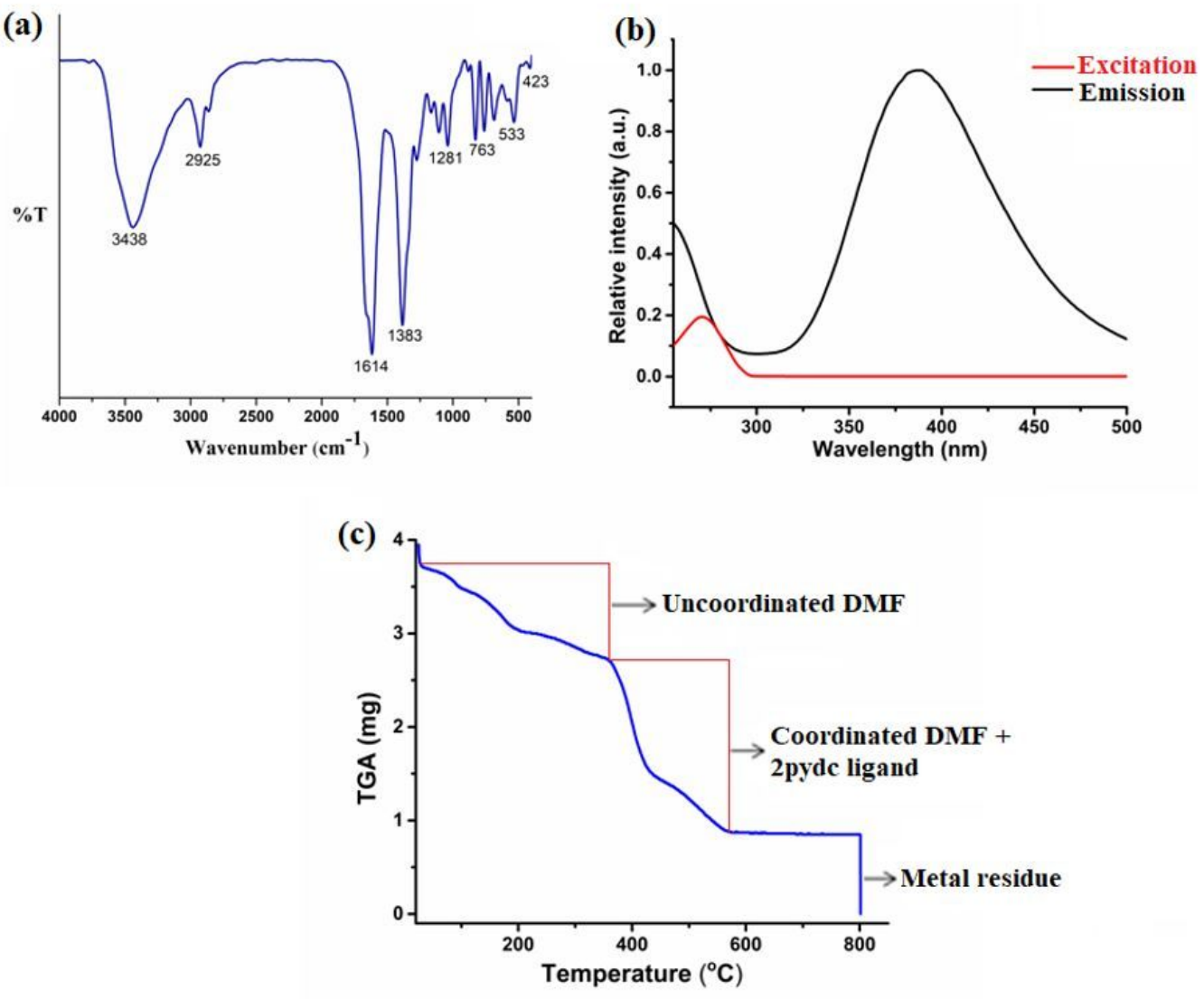

Figure 4

(a) FTIR spectra of Zn-MOF-1. (b) Absorption and Emission spectrum of Zn-MOF-1. (c) TG Analysis of Zn-MOF-1.

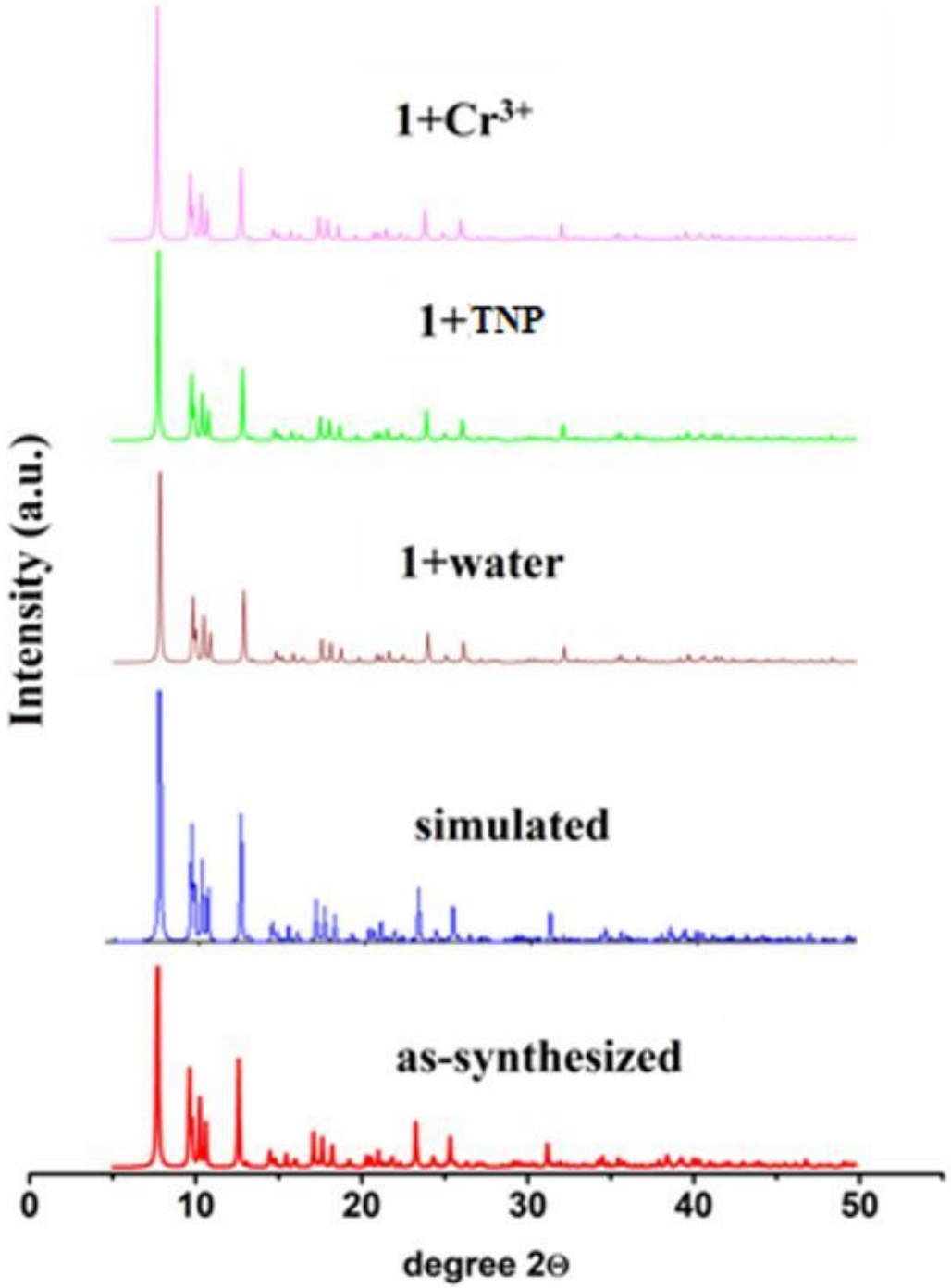

Figure 5

PXRD pattern of Zn-MOF-1 as synthesized, simulated, in water, in TNP and in Cr3+ ion.

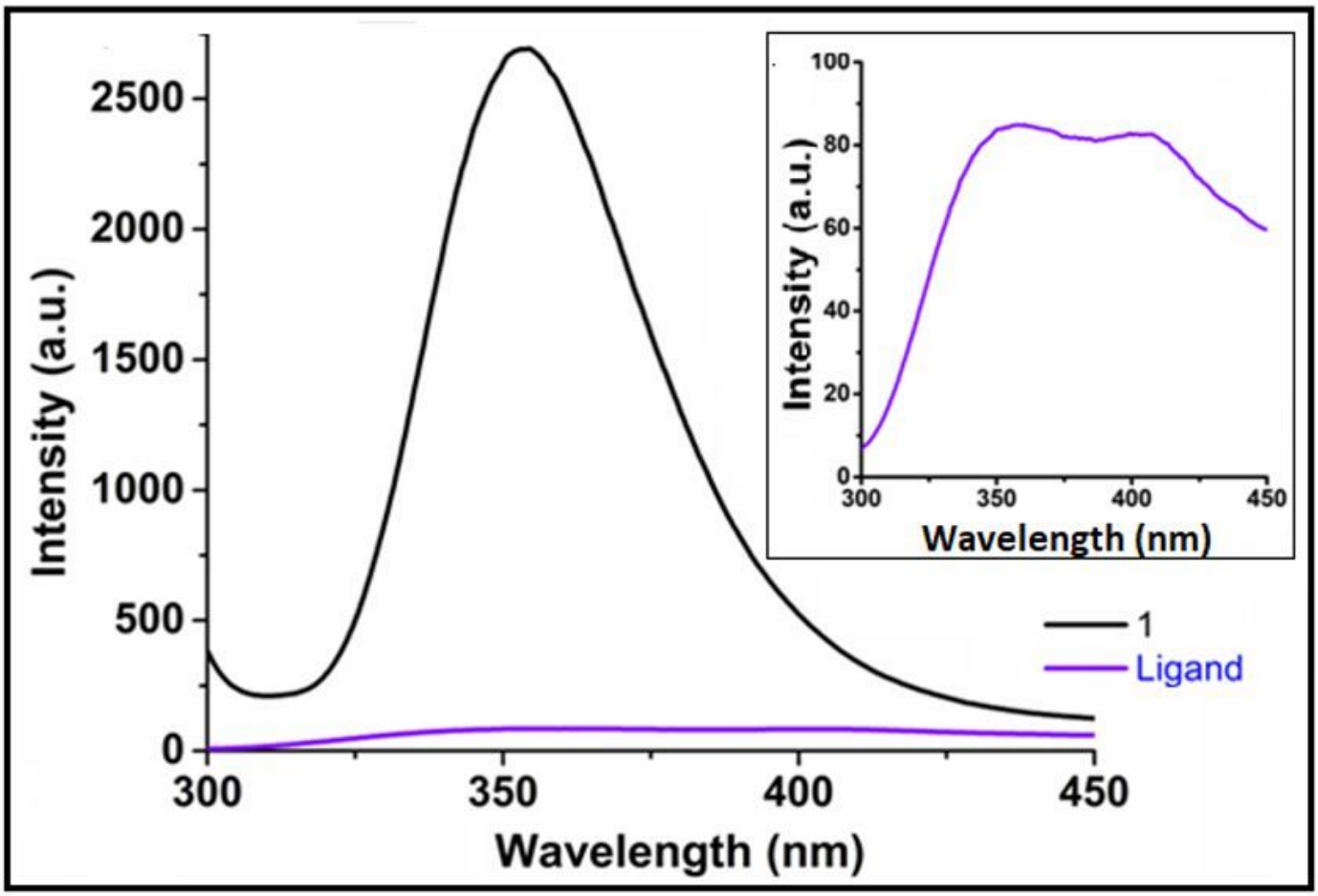

Figure 6

Emission spectrum of Zn-MOF-1 and pydc ligand (Inset: Emission spectrum of ligand upon excitation at 270 nm).

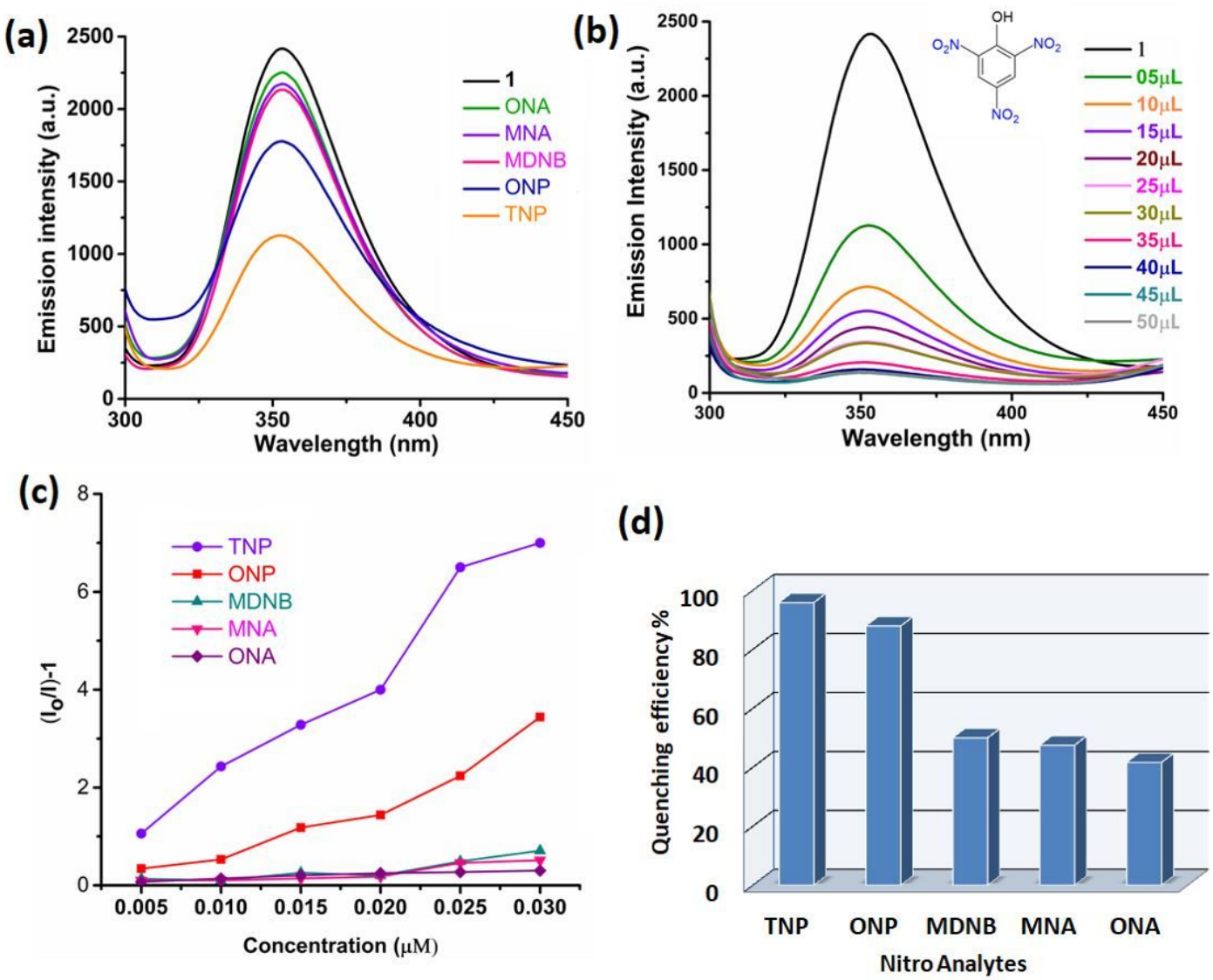

Figure 7

(a) The change in fluorescence intensity of Zn-MOF-1 (λex = 272 nm) upon addition of 5μl of different nitro analytes. (b) The change in fluorescence intensity of Zn-MOF-1 on incremental addition of TNP. (c) Stern-Volmer plot of various nitro analytes. (d) % Quenching efficiency of various nitro analytes in presence of Zn-MOF-1.

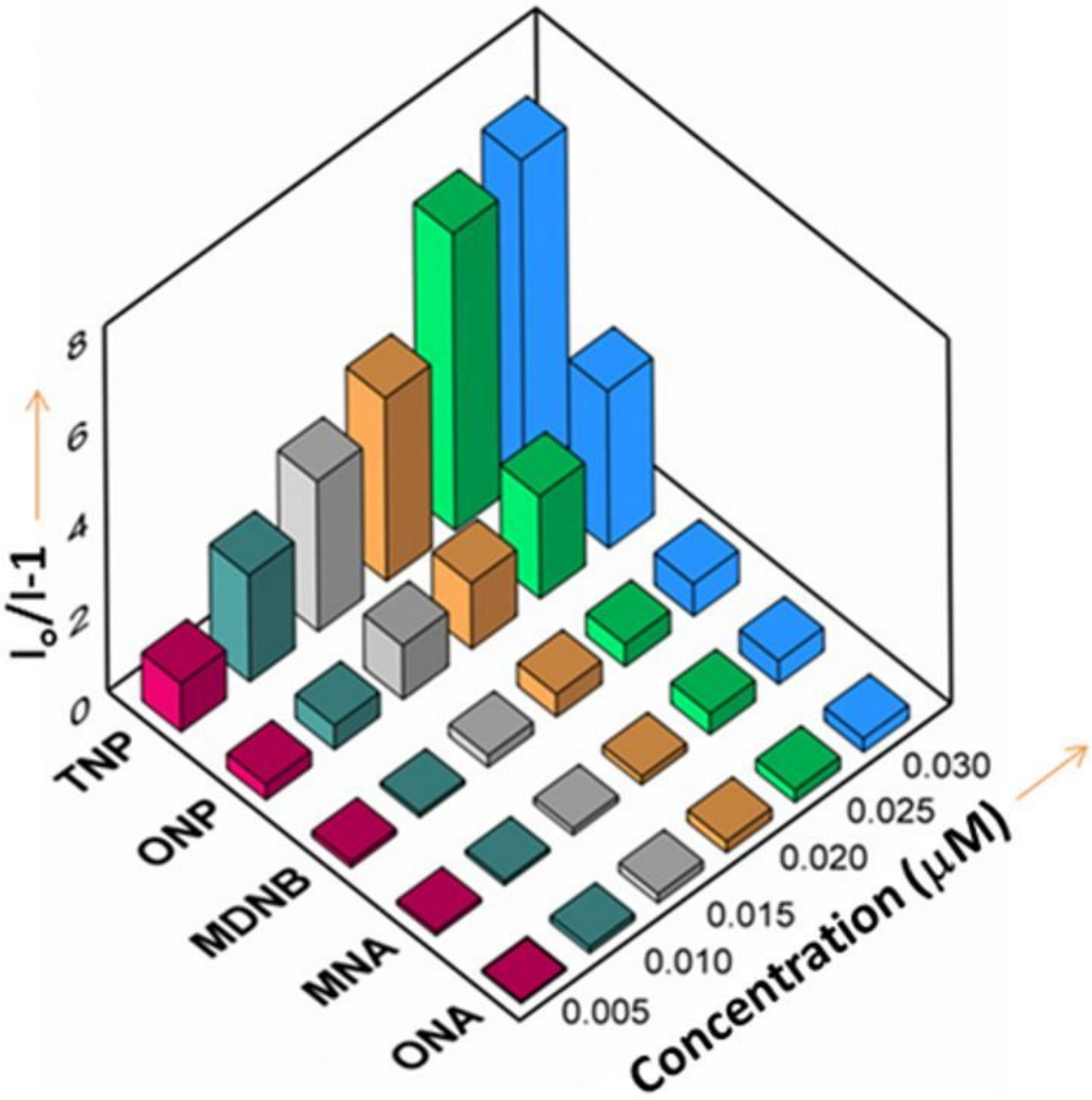

Figure 8

3D Stern-Volmer plot of various nitro analytes in water for Zn-MOF-1.

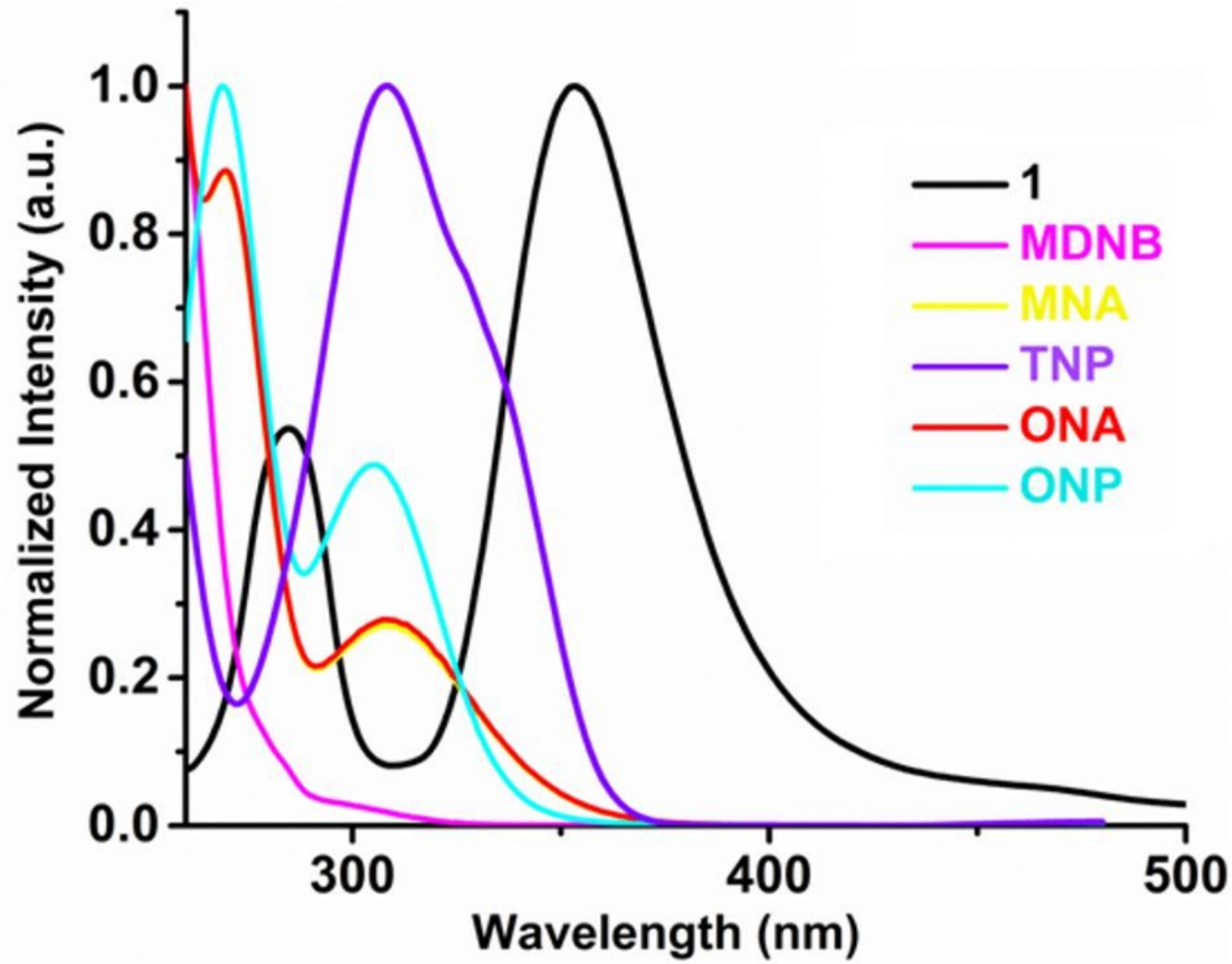

Figure 9

Spectral overlap between normalized emission spectra of Zn-MOF-1 (λex = 272 nm) and normalized absorbance spectra of nitro analytes.

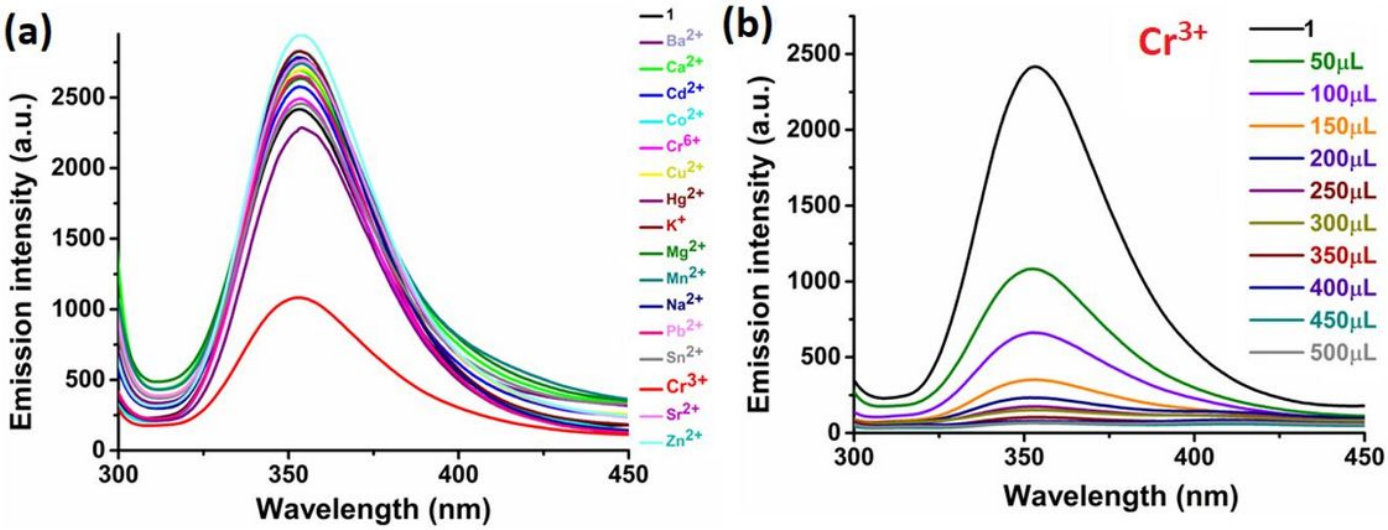

Figure 10

(a) The change in fluorescence intensity of Zn-MOF-1 (λex = 272nm) upon addition of different metal cations. (b) The change in fluorescence intensity of Zn-MOF-1 with incremental addition of Cr3+.

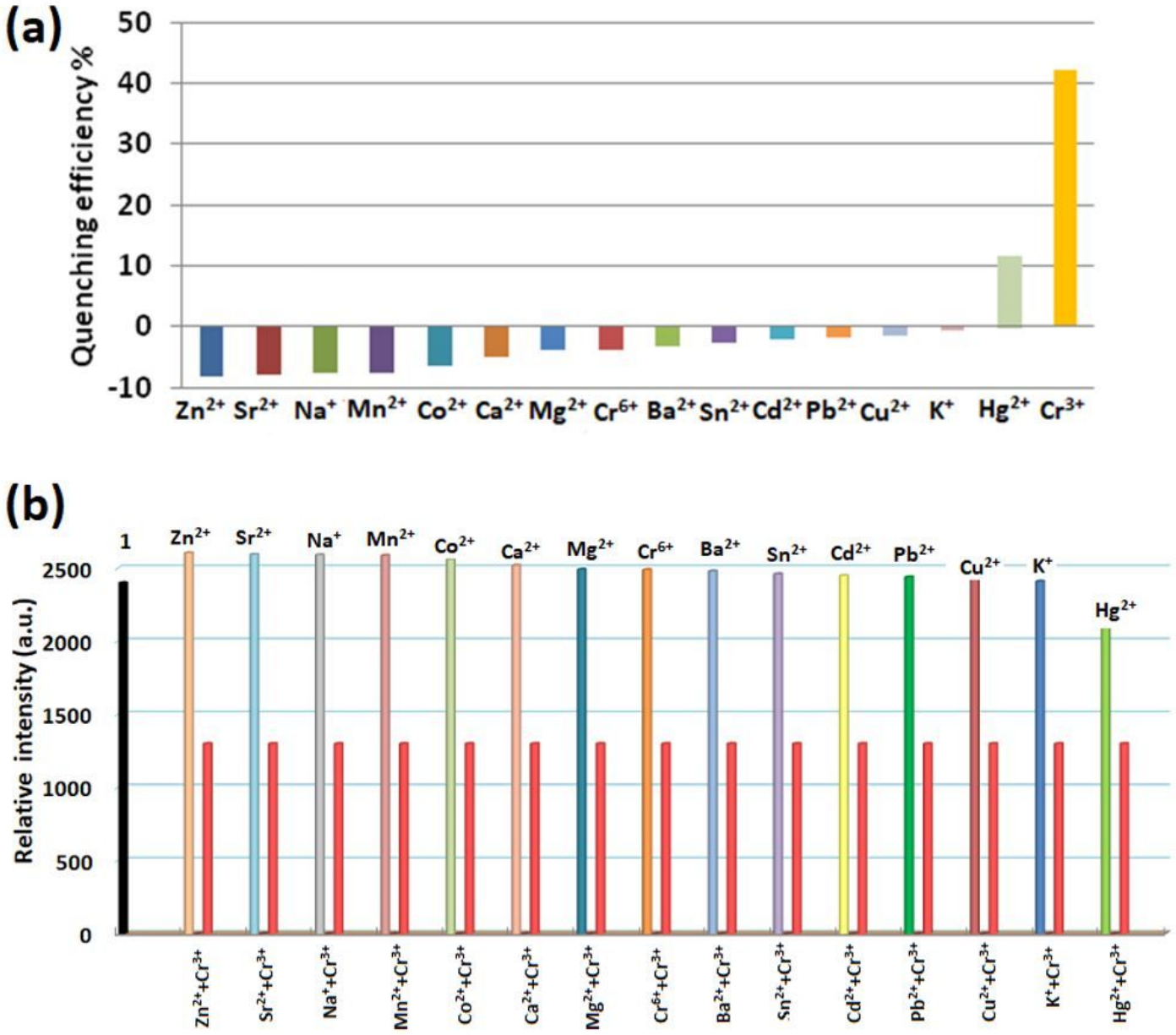

Figure 11

(a) The fluorescence quenching efficiencies of different analytes upon addition of 50µl in Zn-MOF-1, (b) Change in fluorescence intensity of Zn-MOF-1 upon addition of different metal ion solution followed by Cr3+ solution respectively in water.

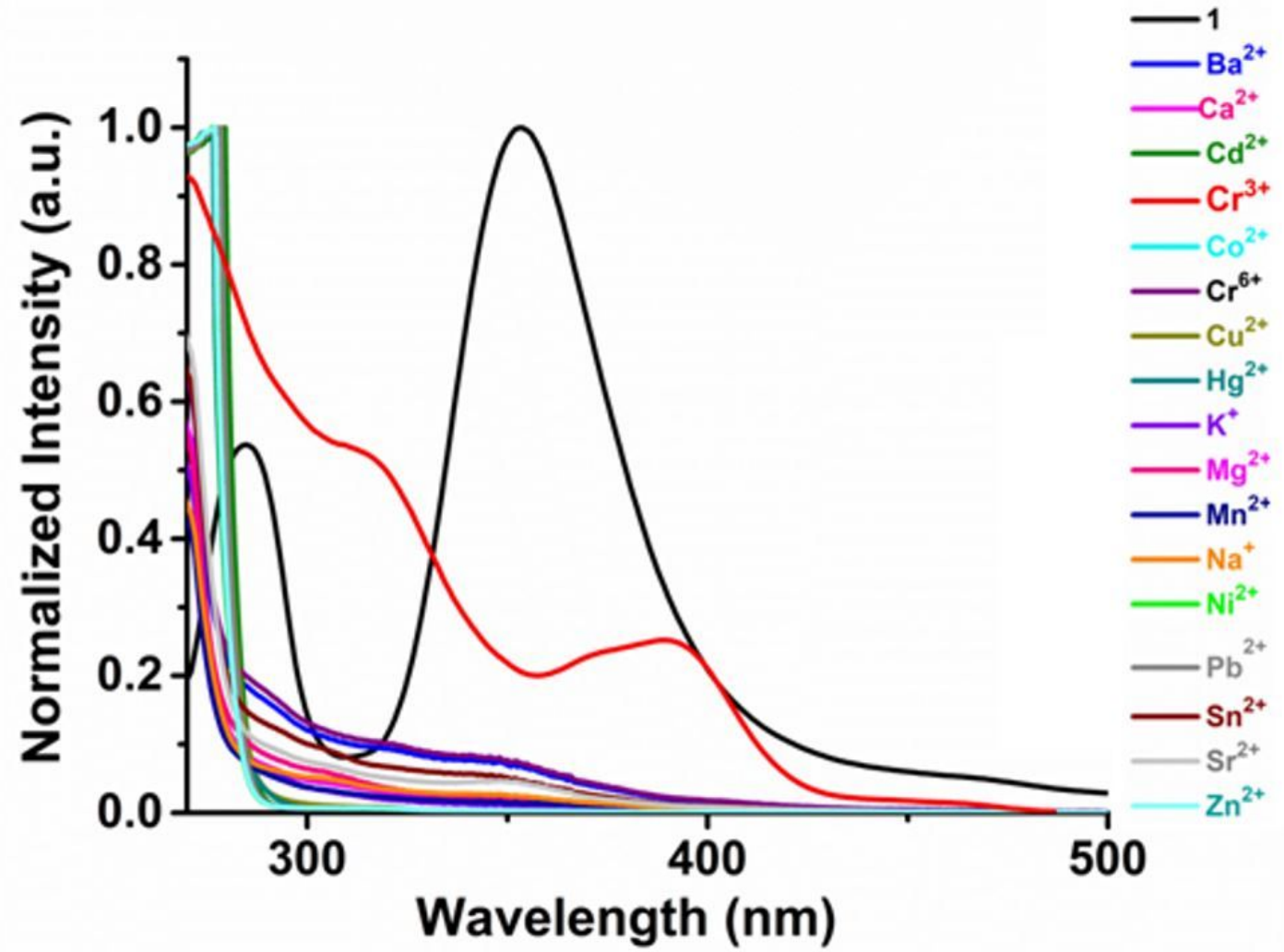

Figure 12

Spectral overlap between normalized emission spectra of Zn-MOF-1 (λex = 272 nm) and normalized absorbance spectra of metal ions.

Supplementary Files

This is a list of supplementary files associated with this preprint. Click to download.

- scheme1.jpg
- scheme2.jpg
- ESIfile.docx
- GRAPHICALABSTRACTpictogram.docx
- GraphicalAbstractSynopsis.docx